[8]See, for example, M. J. Seaton, Proc. Phys. Soc. (London) 88, 815 (1966); and D. L. Moores, *ibid.* 88, 843 (1966).

[9]P. G. Burke and H. M. Schey, Phys. Rev. 126, 147 (1962). This fact is also well known in nuclear and particle physics.

[10]C. E. Moore, *Atomic Energy Levels* (U. S. Natl. Bur. Std., Washington, D. C., 1958), Circ. No. 467, Vol. III.

[11]K. Yoshino, Optical Society of America 1969 Annual Meeting program No. WH12 (unpublished); K. Yoshino (unpublished). (We express our appreciation to Dr. Yoshino for allowing us full use of the data before formal publication.)

[12]H. Beutler, Z. Physik 93, 177 (1935); F. J. Comes and H. G. Sälzer, Phys. Rev. 152, 29 (1966).

[13]J. Macek, Phys. Rev. A 1, 618 (1970); and see, for example, P. G. Burke, J. W. Cooper, and S. Ormonde, *ibid.* 183, 245 (1969).

[14]Reference 10, Vol. II (1952).

[15]W. R. S. Garton and K. Codling, Proc. Phys. Soc. (London) 75, 87 (1960); W. R. S. Garton and F. S. Tomkins, Astrophys. J. 158, 1219 (1969).

[16]U. Fano and J. Cooper, Rev. Mod. Phys. 40, 441 (1968).

[17]M. J. Seaton, J. Phys. B2, 5 (1969).

PHYSICAL REVIEW A VOLUME 2, NUMBER 1 JULY 1970

Experiments on the 2^3P State of Helium. II. Measurements of the Zeeman Effect*

S. A. Lewis,† F. M. J. Pichanick,‡ and V. W. Hughes

Physics Department, Yale University, New Haven, Connecticut 06520

(Received 17 December 1969)

A series of Zeeman resonances has been measured in the 2^3P state of He^4, using the optical-microwave atomic-beam magnetic-resonance technique. The results were analyzed in terms of relativistic and motional contributions to the Zeeman effect, and are presented in the form of corrected g factors: $g_{S'} = g_S - (76.0 \pm 2.4) \times 10^{-6}$, $g_{L'} = g_L + (3.8 \pm 9.0) \times 10^{-6}$, and an additional factor $g_x = (4.0 \pm 25.0) \times 10^{-6}$. These are compared with theoretical calculations using quasi-hydrogenic radial wave functions which give $g_{S'} = g_S - (79.9 \pm 3.5) \times 10^{-6}$, $g_{L'} = g_L + (1.1 \pm 1.5) \times 10^{-6}$, and $g_x = -(3.2 \pm 4.4) \times 10^{-6}$. The values of the experimental g factors are $g_S^1 = 2.002\,243\,2 \pm 0.000\,022\,4$, and $g_L^1 = 0.999\,867 \pm 0.000\,009$. The validity of the theory and the consistency of the data are discussed. The experimental results were used to reduce the quoted uncertainty in a previously reported fine-structure measurement. The new result is $E(2^3P_1) - E(2^3P_2) = 2291.196 \pm 0.005$ MHz.

I. INTRODUCTION

A previous paper[1] (referred to as I) reported a measurement of the $2^3P_1 - 2^3P_2$ fine-structure interval of helium to a precision of 3 ppm. The most accurate data were taken in a magnetic field of 500 G, and the evaluation of the fine structure required some assumptions about the 2^3P g factors. Relativistic and motional contributions to these g factors were calculated using quasihydrogenic radial wave functions. The nature of the radial integrals involved was such that the g-factor calculations contributed a significant portion of the experimental uncertainty quoted for the fine structure. For this reason, and because of an intrinsic interest in the Zeeman effect of the 2^3P state of helium, we decided to measure the g factors directly.

In this paper, we report measurements of the 2^3P g factors (including factors off diagonal in J) to a precision of about 10 ppm. These g factors occur in matrix elements of the Zeeman Hamiltonian expressed in a (J, m_J) representation. They were expressed in terms of unknown radial integrals arising from relativistic and motional contributions, and their values were deduced from measurements of a series of magnetic dipole transitions between Zeeman sublevels. A brief report of this work has been given.[2]

The relativistic contributions have been derived theoretically from the Dirac-Breit equation by Perl and Hughes.[3] A generalization for many-electron atoms was presented by Perl,[4] and by Abragam and van Vleck.[5] Several comparisons with experiment have been made utilizing this theory. The measurement[6] of g_J (He; 2^3S_1) agrees to within 1 ppm with theory,[3] where most of the relativistic contributions could be evaluated in terms of known quantities, and detailed radial wave functions were not required. In more complicated atoms, the relevant radial integrals are evaluated usually with Hartree-Fock wave functions. Detailed comparisons have been made, for instance, in the $^2P_{3/2}$ state of fluorine[7] (agreement to within 1 ppm), and in the ^3P states of oxygen[8] (agreement to 7 ppm).

The present work differs from those above in that the Zeeman transitions observed had line-

widths of about 5 MHz. The use of much higher magnetic fields was necessary in order to obtain a reasonably large ratio of transition frequency to linewidth. At these fields, terms quadratic in field, and relativistic contributions off diagonal in J were appreciable and lent further interest to the experiment. Furthermore, some of the terms in the Dirac-Breit Hamiltonian, which do not contribute to the Zeeman effect in the 2^3S state of helium, are nonzero in the case of the 2^3P states.

The experiments were performed using the atomic-beam optical-microwave magnetic-resonance technique.[9] The 2^3P states were excited optically from the 2^3S_1 state in the C (uniform) magnetic field of an atomic-beam spectrometer (Fig. 1)[10]. Magnetic dipole resonance transitions between the 2^3P Zeeman sublevels were observed by their contribution to the redistribution of 2^3S_1 sublevel populations after 2^3P decay. The relevant energy levels and their role in the experiment are depicted in Fig. 2. The beam of metastable 2^3S_1 atoms was obtained by electron-impact excitation from the 1^1S_0 ground state. The apparatus had oppositely directed A- and B-field gradients which, together with a collimator, defined the $m_S = +1$, 0, -1 trajectories reaching the detector, as shown in Fig. 1. Between the A and B magnets was the uniform C field, wherein occurred transitions between the m_S sublevels. These transitions arose from the optical excitation to the 2^3P sublevels and the subsequent decay back to 2^3S_1, and they were modified by magnetic dipole resonances between the 2^3P sublevels. It was desirable to select transitions between specific 2^3S_1 (m_S) sublevels, so as to enhance our sensitivity for observing the 2^3P resonances. This was accomplished by placing a second collimator (state selector) near the B field, and by moving the detector to one side. Figure 1 illustrates the configuration for observation of the 2^3S_1 ($m_S = 0 \rightarrow +1$) transition. It should be pointed out that the 2^3P sublevels could only decay to 2^3S_1, decay to the 1^1S_0 ground state being strictly forbidden. The 2^3P radiative lifetime was about 1×10^{-7} sec and the transit time of the atoms through the C region was about 5×10^{-5} sec.

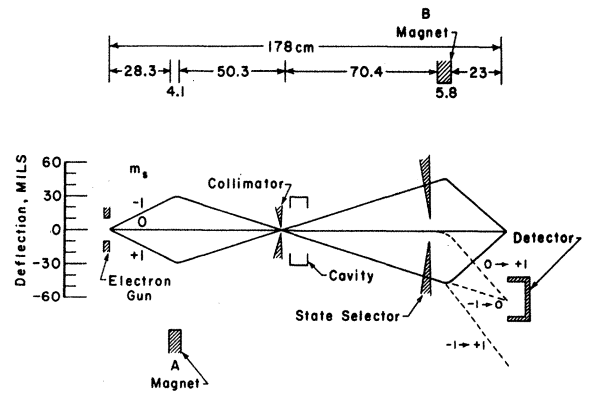

FIG. 1. Diagrammatic plan of the atomic-beam spectrometer illustrating the $2^3S_1(m_S)$ trajectories. Broken lines near the detector are trajectories of atoms undergoing changes in m_S as indicated by the labeling. Atoms originating in $m_S = \pm 1$ would normally hit the state selector. The microwave cavity was situated in the C field.

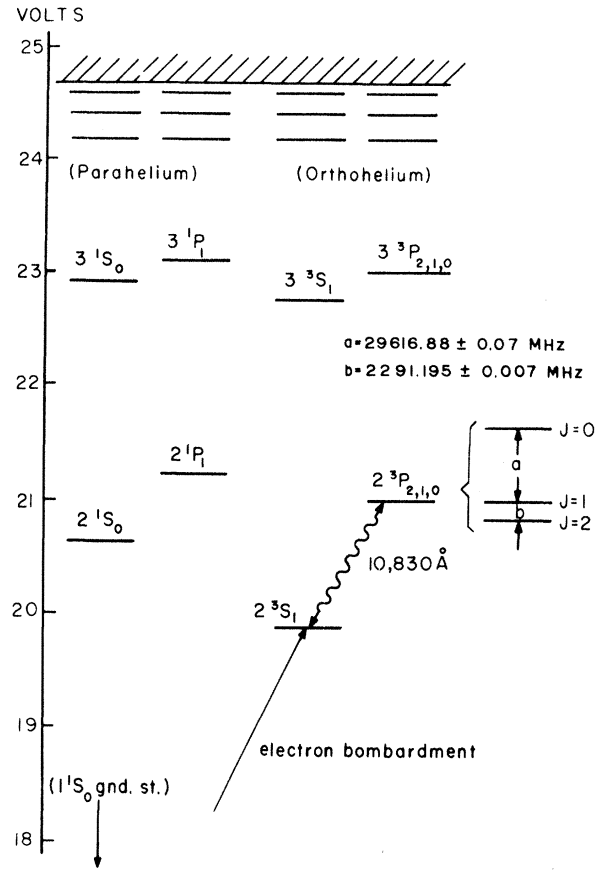

FIG. 2. Energy-level diagram of the helium atom. The $^1S_0$ ground state, which lies 19.82 eV below the state 2^3S_1, has been omitted. The experimental processes of electron and optical excitation are depicted by arrows. The 2^3P fine structure (not to scale) is shown in detail.

II. THEORY OF EXPERIMENT

A. Zeeman Hamiltonian

The theory presented in I is expanded here to include the relativistic, motional, and quadratic contributions from the beginning, rather than introducing them as additional perturbations later on. We consider only the perturbation Hamiltonian resolving the degeneracy of the 2^3P state which we write

$$\vec{\mathcal{H}} = \vec{\mathcal{H}}_{FS} + \vec{\mathcal{H}}_Z + \vec{\mathcal{H}}_Q \ . \tag{1}$$

$\vec{\mathcal{H}}_{FS}$ includes the spin-orbit and spin-spin terms which lead to the fine structure.[11] It is diagonal in J, and hence we shall employ as a matrix representation the zero-field eigenstates $|LSJm_J\rangle$. $\vec{\mathcal{H}}_Z$ represents the linearly field-dependent (Zeeman) terms and $\vec{\mathcal{H}}_Q$ the quadratically field-dependent terms. When solving the secular equation, the contribution of $\vec{\mathcal{H}}_{FS}$ will be represented by constant diagonal terms E_J, the zero-field eigenvalues for $J=0$, 1, and 2. This procedure[12] allows for the admixture of $\vec{\mathcal{H}}_{FS}$ of the 2^1P_1 state to the required accuracy (see Appendix C A). The values of E_J will be based on the experimental values of the fine structure intervals.[13]

The linear Zeeman term can be written

$$\vec{\mathcal{H}}_Z = g_L \ \mu_B \ \vec{L}\cdot\vec{H} + g_S \mu_B \vec{S}\cdot\vec{H} + \sum_{r=1}^{6} \vec{\delta}\vec{\mu}_r \cdot \vec{H}, \tag{2}$$

where μ_B is the Bohr magneton. $\vec{L}$, $\vec{S}$ are, respectively, the total orbital and spin angular momentum operators in units of $\hbar$. The first two terms are, respectively, the usual interaction of the orbital and spin magnetic moments with the external magnetic field H, which is assumed to be in the z direction. The orbital and spin g factors are assumed to have the values

$$\begin{aligned} g_L &= (1 - m/M) = 0.999\,862\,9\ , \\ g_S &= 2(1 + (\alpha/2\pi) - 0.328\ (\alpha^2/\pi^2)\cdots) = 2.002\,319\,2. \end{aligned} \tag{3}$$

m, M are, respectively, the electronic and nuclear masses, and the above expression for g_L includes most of the correction for nuclear motion. There is a smaller more complicated motional correction which we have included in the third term of Eq. (2). α is the fine structure constant $e^2/\hbar c$. The expression for g_S arises from the theoretical evaluation of the anomalous electron moment,[14] and the difference between this number and the most recent experimental value[15] is negligible for our purposes.

The first five of the $\vec{\delta}\vec{\mu}_r$ are the relativistic corrections given by

$$\begin{aligned} \vec{\delta}\vec{\mu}_{1,2} &= -\frac{1}{mc^2}\ \mu_B \\ &\quad \times \sum_i \{(\vec{l}_i + 2\vec{s}_i)\, T_i - \tfrac{1}{2} Ze^2[\vec{s}_i \times \vec{\nabla}_i(r_i^{-1})] \times \vec{r}_i\}\ , \\ \vec{\delta}\vec{\mu}_{3,4} &= -\frac{e^2}{mc^2}\ \mu_B \\ &\quad \times \sum_{i<j} [(\vec{s}_i + 2\vec{s}_j) \times \vec{\nabla}_i(r_{ij}^{-1})] \times \vec{r}_i\ , \\ \vec{\delta}\vec{\mu}_5 &= -\frac{e^2}{\hbar mc^2}\ \mu_B \\ &\quad \times \sum_{i<j} [r_{ij}^{-1}(\vec{r}_i \times \vec{p}_j) + r_{ij}^{-3}\,(\vec{r}_i \times \vec{r}_j)(\vec{r}_{ij}\cdot\vec{p}_j)]\ , \end{aligned} \tag{4a}$$

where $\vec{l}_i$, $\vec{s}_i$ are, respectively, the orbital and spin angular momentum operators for the ith electron, T_i is the kinetic-energy operator, and $\vec{r}_i\,(\vec{r}_j)$ is the spatial coordinate operator for the ith (jth) electron with $\vec{r}_{ij} = \vec{r}_j - \vec{r}_i$. Z is the atomic number.

$\delta\mu_6$ is the additional motional correction[16] mentioned above:

$$\vec{\delta}\vec{\mu}_6 = -\frac{m}{M}\ \mu_B \sum_{i<j} [(\vec{r}_i \times \vec{p}_j) + (\vec{r}_j \times \vec{p}_i)]\ . \tag{4b}$$

The quadratic term in Eq. (1) is

$$\vec{H}_Q = \frac{e^2}{8mc^2} \sum_i (\vec{H}\times\vec{r}_i)\cdot(\vec{H}\times\vec{r}_i)\ . \tag{5}$$

The first step in evaluating the 2^3P energy eigenvalues as a function of magnetic field is to determine the matrix elements of the Hamiltonian [Eq. (1)] in the $|LSJm_J\rangle$ scheme. We have done this using a spherical-tensor-recoupling scheme following Innes and Ufford,[8] and the details of this calculation are given in Appendix A. The complete matrix, which is block diagonal in m_J is given in Table I. Configuration interaction was neglected in the evaluation of this matrix (see Sec. VI). The factors g_s', g_L', and g_x are essentially the quantities measured in this experiment. They are defined in Appendix A, Eq. (14), in terms of the known quantities g_s, g_L and the unknown radial integrals which are parts of the matrix elements of the $\vec{\delta}\vec{\mu}_i$. The secular equation derived from the Hamiltonian matrix (Table I) is solved as in I, Table II. The resultant energy levels are plotted as a function of magnetic field in Fig. 3. At very high fields where the Zeeman energy greatly exceeds the fine structure intervals, the $|LSm_Lm_S\rangle$ quantum-number scheme is more appropriate, and the energy levels have been thus labeled on the high-field side of the diagram. The $|LSm_Lm_S\rangle$ scheme is also more appropriate for discussion of optical-transition probabilities (see Sec. II B). At any finite field the only "good" quantum number is $m_J = m_L + m_S$. In Fig. 4, we show the $J=1,2$ energy levels in more detail, but not to scale, and the double arrows depict some of the magnetic dipole transitions relevant to this experiment. The numbering of the transitions is a scheme due to Lamb.[12] The frequencies of these transitions are plotted in Fig. 5, and for later reference (Appendix C D) we have included the 2^3S_1 Zeeman frequency.

B. Optical-Transition Probabilities

As in I, we label the 2^3P eigenfunctions as $\psi(\mathcal{J}m_J)$ where $\mathcal{J}$ represents the value of J to which an eigenstate belongs at zero field (i.e., the script $\mathcal{J}$ denotes that J is not a "good" quantum number at finite magnetic field). The $\psi(\mathcal{J}m_J)$ are written as linear combinations of the products of eigenfunctions of $\vec{L}_z$ and $\vec{S}_z$:

TABLE I. Hamiltonian matrix for ^3P.

$m_J=0$			
J \ J'	0	1	2
0	$E_0+Q(R_{14}+R_{15})$	$-(\frac{2}{3})^{1/2}(g_S'-g_L'+\frac{1}{6}g_x)\mu_BH$	$(\frac{2}{25})^{1/2}QR_{15}$
1	$-(\frac{2}{3})^{1/2}(g_S'-g_L'+\frac{1}{6}g_x)\mu_BH$	$E_1+Q(R_{14}+\frac{6}{5}R_{15})$	$-(\frac{1}{3})^{1/2}(g_S'-g_L'-\frac{2}{15}g_x)\mu_BH$
2	$(\frac{2}{25})^{1/2}QR_{15}$	$-(\frac{1}{3})^{1/2}(g_S'-g_L'-\frac{2}{15}g_x)\mu_BH$	$E_2+Q(R_{14}+\frac{4}{5}R_{15})$
$m_J=\pm1$			
J \ J'	1	2	
1	$E_1+Q(R_{14}+\frac{9}{10}R_{15})\pm\frac{1}{2}(g_S'+g_L'-\frac{1}{3}g_x)\mu_BH$	$\pm\frac{3}{10}QR_{15}-\frac{1}{2}(g_S'-g_L'-\frac{2}{15}g_x)\mu_BH$	
2	$\pm\frac{3}{10}QR_{15}-\frac{1}{2}(g_S'-g_L'-\frac{2}{15}g_x)\mu_BH$	$E_2+Q(R_{14}+\frac{9}{10}R_{15})\pm\frac{1}{2}(g_S'+g_L'+\frac{1}{15}g_x)\mu_BH$	
$m_J=\pm2$			
J \ J'	2		
2	$E_2+Q(R_{14}+\frac{6}{5}R_{15})\pm(g_S'+g_L'+\frac{1}{15}g_x)\mu_BH$		

$Q=(\mu_0H)^2/6R_\infty$; $E_1-E_2=2291.196\pm0.005$ MHz; $E_0-E_1=29\,616.88\pm0.07$ MHz.

$$\psi(\mathcal{J}m_J)=\sum_{m_S}\{m_Sm_L|\mathcal{J}m_J\}\Phi(m_L)\chi(m_S)\ . \qquad (6)$$

Equation (6) defines the coupling coefficients $\{m_Sm_L|\mathcal{J}m_J\}$ which were evaluated in I. We have from I the following expressions for $\sigma(m_S;\mathcal{J},m_J)$, the relative probability for excitation from $2^3S(m_S)$ to $2^3P(\mathcal{J},m_J)$ by a plane wave traveling in the y direction with polarization uniformly distributed in the xz plane, and for $\gamma(\mathcal{J},m_J;m_S')$, the relative probability for radiative decay from $2^3P(\mathcal{J},m_J)$ to $2^3S(m_S')$:

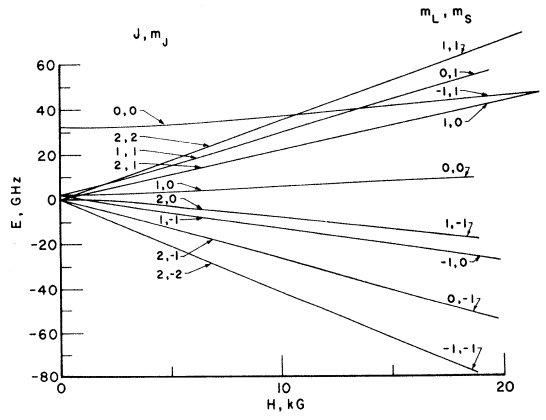

FIG. 3. Energy levels of 2^3P as a function of magnetic field. On the left-hand (low-field) side of the figure the levels are labeled according to the quantum numbers J, m_J. On the right-hand (high-field) side the quantum numbers m_S, m_L are more appropriate.

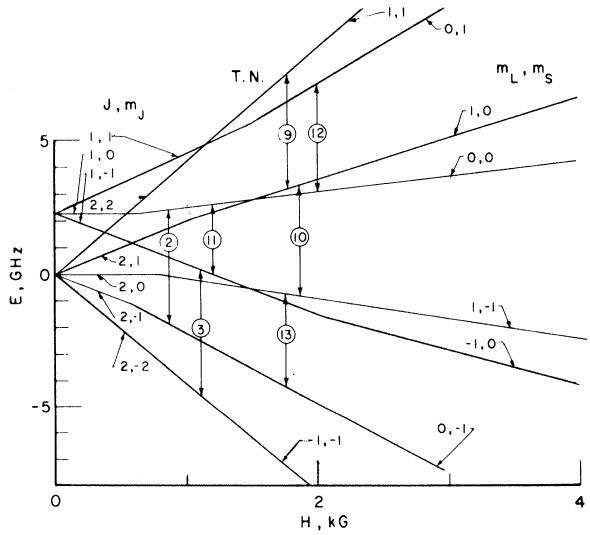

FIG. 4. Detail of the 2^3P, $J=1$, and 2, energy levels as a function of magnetic field. The double arrows with numbered circles indicate magnetic dipole transitions of experimental interest.

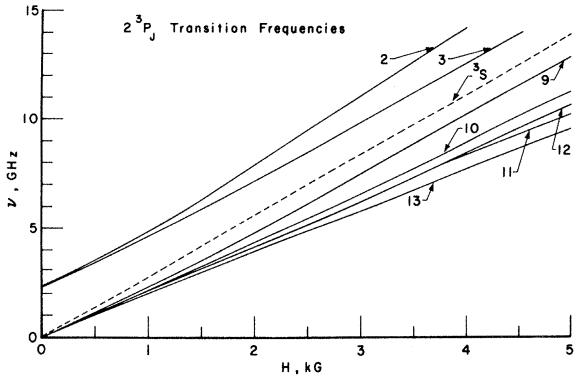

FIG. 5. Frequencies of the 2^3P magnetic dipole transitions as a function of magnetic field. The numbers correspond to the labeling in Fig. 4. The broken line is the 2^3S_1 Zeeman frequency.

$$\sigma(m_s; \mathcal{J} m_J) = I(\mathcal{J})\{m_S, m_J - m_S \mid \mathcal{J} m_J\}^2,$$
$$\times \tfrac{1}{2} \text{ for } m_J - m_S = \pm 1 \qquad (7)$$
$$\times 1 \text{ for } m_J - m_S = 0,$$
$$\gamma(\mathcal{J}, m_J; m_S') = \{m_S' \mid \mathcal{J}, m_J\}^2,$$

where the $I(\mathcal{J})$ are spectral weighting factors appropriate to the excitation source (see Fig. 6).

In I, the values of these relative probabilities were illustrated for $\vec{H} = 0$. In the present work, it is more instructive to consider them for $\vec{H} = \infty$, and they are thus depicted in Fig. 7. In this figure,

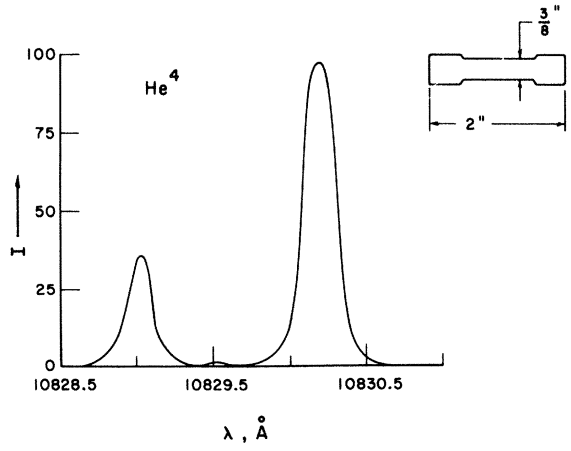

FIG. 6. Spectral intensity distribution of a typical excitation lamp. The small peak at lower wavelength arises from the $2^3P_0 \rightarrow 2^3S_1$ transition, and the larger peak from the unresolved 2^3P_1, $2^3P_2 \rightarrow 2^3S_1$ components. The inset gives the lamp dimensions.

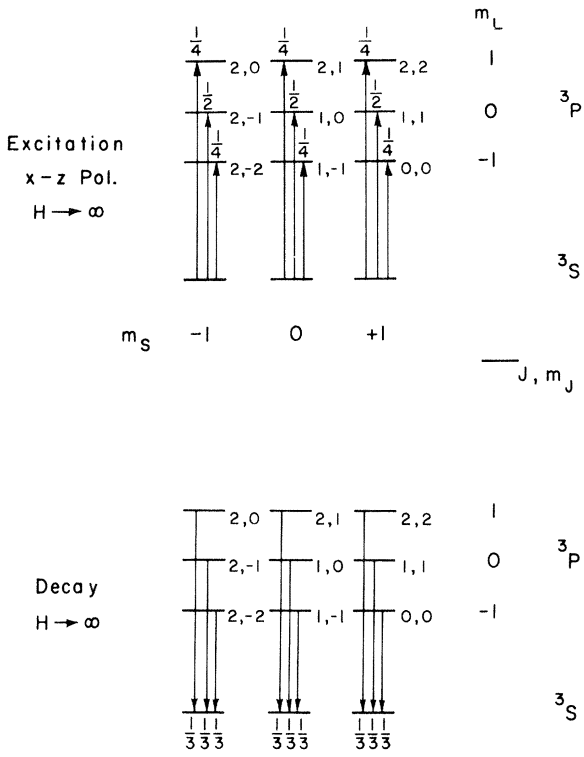

FIG. 7. Diagrammatic representation of the 2^3S-2^3P optical excitation and decay probabilities in the high-field limit. The levels are ordered according to the high-field quantum numbers m_L, m_S, whereas each ^3P level is individually labeled with its low-field quantum number J, m_J. The value of the relative probability is written as a fraction at the end of each arrow.

the levels are ordered in terms of $^3P(m_S, m_L)$, the "good" quantum numbers at infinite field; the electric dipole selection rules $\Delta m_S = 0$, $\Delta m_L = 0, \pm 1$ are clearly illustrated. The value of a relative probability is written as a fraction at the end of each arrow. No spectral weighting has been included, and multiplicative factors have been used such that the total probability for emanating from, or decaying to, a particular $2^3S(m_S)$ sublevel is unity. The individual 2^3P sublevels have been labeled also by their corresponding zero-field "good" quantum numbers $(\mathcal{J}, m_J)$. At intermediate fields levels of the same m_J (located along diagonals in Fig. 7) are admixed.

C. rf Transitions

In the Sec. I, we pointed out that rf Zeeman transitions between a pair of 2^3P sublevels α, β were observed as a change in the rate of transfer from $2^3S_1(m_S)$ to $2^3S_1(m_S')$ after optical excitation and decay. In I, the following expression for the relative signal strength was derived:

$$S(^{\alpha\to\beta}_{m_S\to m_S'}) = \frac{\rho(\alpha,\beta)\,[\sigma(m_S;\beta)-\sigma(m_S;\alpha)]\,[\gamma(\alpha;m_S')-\gamma(\beta;m_S')]}{\sum_{\mathcal{J},m_J}\sigma(m_S;\mathcal{J},m_J)\,\gamma(\mathcal{J}m_J;m_S')}\,, \tag{8}$$

where the line-shape function is given by the Lorentzian

$$\rho(\alpha,\beta) = \frac{2(\mu_0 H_1)^2|V|^2}{(\omega_{\alpha\beta}-\omega)^2+4(\mu_B H_1)^2|V|^2+\gamma^2}\,. \tag{9}$$

Here we have assumed an applied rf magnetic field of frequency ω:

$$\vec{H}_1 = 2\vec{h}_1 H_1 \cos\omega t, \tag{10}$$

$\vec{h}_1$ being a unit vector specifying the direction of $\vec{H}_1$. V is the matrix element $\langle\alpha|g_S\vec{S}+g_L\vec{L})\cdot\vec{h}_1|\beta\rangle$, $\omega_{\alpha\beta}$ is the resonant frequency $|(E_\alpha - E_\beta)|/\hbar$, and γ is the decay rate (about 1×10^7/sec) of the 2^3P state. The middle term in the denominator of Eq. (9) represents the power broadening, and the optimum linewidth $\Delta\nu$ (frequency units) occurs when $\rho(\alpha,\beta)/\Delta\nu$ is maximum:

$$\begin{aligned}&\Delta\nu\ (\text{optimum}) = \sqrt{3}\gamma/\pi \sim 5.5\ \text{MHz}\,,\\ &2H_1\ (\text{optimum}) = \sqrt{2}\gamma/(\mu_B|V|)\sim 1\text{–}2\ \text{G}\end{aligned} \tag{11}$$

for the rf transitions involved. The Zeeman transitions observed in this experiment had $\Delta m_J = \pm1$, and $\vec{h}_1$ was in the y direction. The $|V|^2$ were evaluated at a particular magnetic field $\vec{H}$ using the coupling coefficients defined in Eq. (6).

Transitions were observed by detecting atoms initially in $2^3S_1(m_S=0)$ and transferring to $2^3S_1\times(m_S'=\pm1)$, and we shall refer to these as $0\to\pm1$ select/detect. The signal [Eq. (8)] was either positive or negative, depending on the relative magnitudes of the optical excitation and decay probabilities involved in a particular rf transition. The signal mechanism is illustrated in Fig. 8, where the vertical arrows represent allowed optical transitions in the high-field limit (Fig. 7) and the curved double arrows represent rf transitions numbered as in Fig. 4. Transitions 9, 12, 10, 2, and 3 connect sublevels in which one of the $\sigma(m_S;\alpha)$ or $\gamma(\alpha;m_S')$ factors is zero while the other is finite, and hence the rf mixing of the sublevels should result in large signals. Transition 13, however, connects sublevels in the same m_S column, and these have comparable decay rates to $2^3S_1(m_S=-1)$ but their excitation rates are small and depend on the amount of intermediate-field admixture. The relative signal from transition 13 therefore is expected to be small. Similar considerations apply to transition 11 with the roles of excitation and decay reversed. The remaining $\Delta m_J=\pm1$ transitions were too small to be detected experimentally.

The calculated signal strengths are plotted in Fig. 9 for $2H_1 = 2G$ as a function of static magnetic field H. Note that transitions 2 and 12 can have negative signals. The signal strengths have been expressed as a percentage of the number of $(0\to\pm1)$ 2^3S_1 transfers with no rf present.

It is important to note that the strongest signals were obtained with high-field quantum number transitions $2^3P(\Delta m_S=\pm1,\ \Delta m_L=0)$. The rf transitions $2^3P(\Delta m_L=\pm1,\ \Delta m_S=0)$ were observable only when the field was not high enough for the 2^3P (m_S, m_L) to be "good" quantum numbers. As a consequence our experiments measured g_S' much more accurately than g_L' (Table I).

III. APPARATUS

A new vacuum system was constructed to fit between the 4.75-in. pole gap of the C magnet described in Sec. III B. The vacuum envelope had a rectangular cross section and was fabricated from

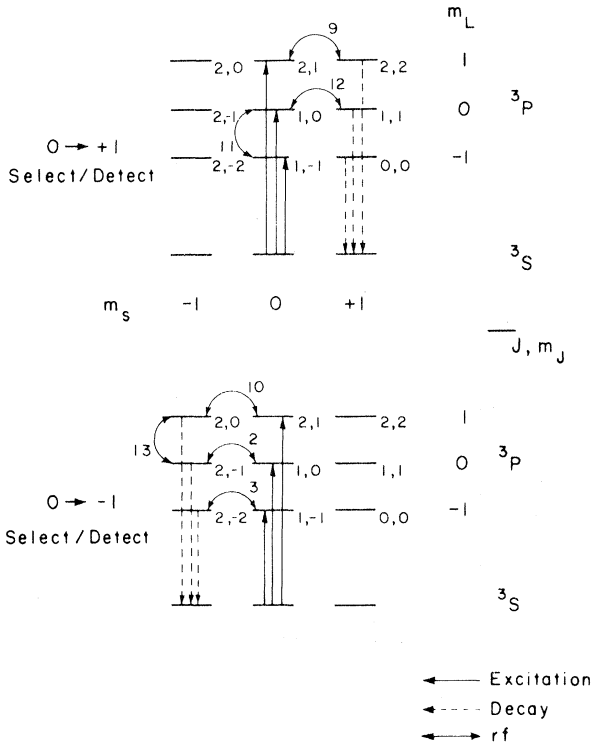

FIG. 8. Illustration of the signal-producing mechanism for $2^3S(m_S=0\to\pm1)$ trajectories. The curved arrows, numbered according to Fig. 4, represent magnetic dipole transitions between 2^3P levels.

welded aluminum plate. The 2^3S_1 source and detector systems were essentially identical to those used in I and will not be described here. The essential dimensions of the apparatus with respect to the atomic trajectories have been given in Fig. 1.

A. Deflecting Magnets

Electromagnets were used having pole faces shaped to simulate a two-wire field in the usual way.[10] The yoke and coils were outside the vacuum system. The pole pieces, which were cylindrical and entered the side faces of the vacuum envelope through O-ring seals, were machined from Hyperco 50. The yokes were made from rectangular bars of Armco. Each magnet had two coils of 830 turns of 3×0.0025-in. aluminum foil interspaced with 3.25×0.0005-in. Mylar tape. A current of 2.5 A through the coils in series provided gradients of 6 kG/cm with a field of about 7 kG at the center of the 0.24-in. gap. Each coil had a resistance of about 3 Ω and no cooling was required.

B. Homogeneous C Field

A Varian electromagnet with 15-in. tapered ring-shim pole tips and a 4.75-in. air gap produced the homogeneous C field. In conjunction with a Hall-probe-regulated current supply it yielded fields of up to 10 kG. The 2^3P rf transitions occurred over an area of about 1 cm^2 where the exciting optical radiation crossed the atomic beam inside the microwave cavity (Fig. 10). Over this area, the C field was uniform to within 2 ppm.

The field was monitored continuously, and was measured by means of a single-coil NMR absorption spectrometer. The probe, located immediately above the microwave cavity (Fig. 10) contained a sample of mineral oil in a 1-mm-diam

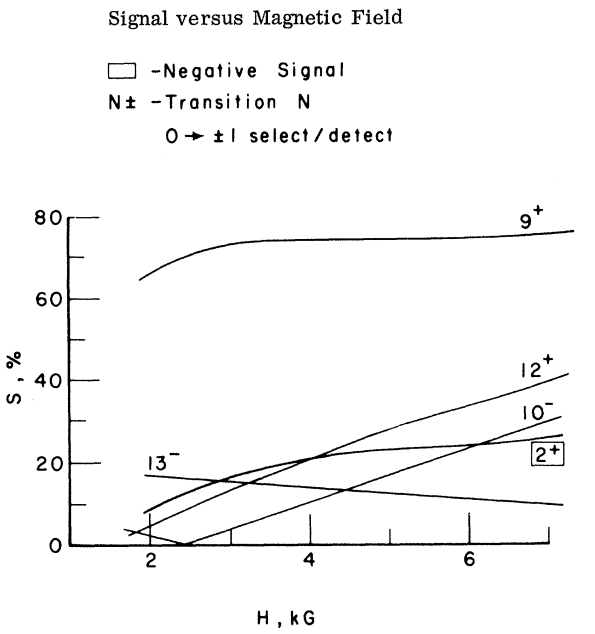

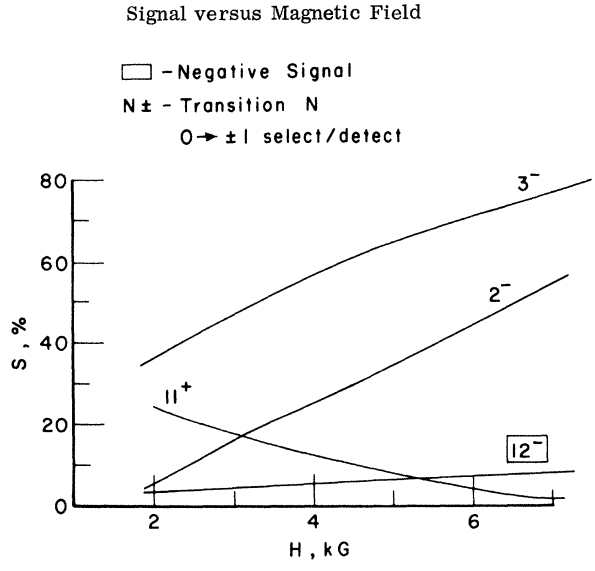

FIG. 9. Calculated 2^3P transition signal intensities as a function of magnetic field. The transitions are numbered according to Fig. 4, and the ± superscripts identify observation with 2^3S ($m_S=0\rightarrow\pm1$) trajectories, respectively.

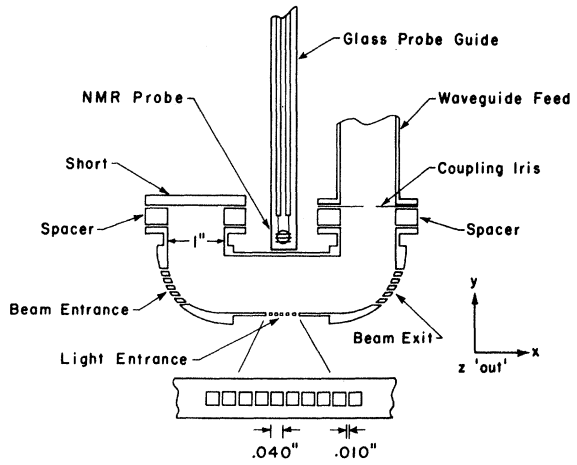

FIG. 10. Cross section of the microwave cavity and NMR probe assembly. The holes for admitting the excitation light are shown in detail at the bottom, and the beam entrance and exit holes were similar. The C field was perpendicular to the diagram.

spherical glass bulb. The over-all diameter of the probe tip, including rf and modulation coils, was about 9 mm. This was inserted into a glass tube, closed at one end, and projected down into the vacuum system. The sealed end rested on top of the microwave cavity as shown in Fig. 10. The center of the proton sample was about 18 mm above the center line of the atomic beam. The C field had been mapped carefully so that the average field over the 2^3P interaction region could be estimated to within 3 ppm. During an experiment, the NMR absorption signal was displayed continuously using phase-sensitive detection, and drifts were controlled to within 1 ppm.

C. Light Source

The commercial helium lamp used in I was replaced by a home-made discharge system. The discharge tube was made of 0.375-in.-diam Pyrex, and was filled with high-purity helium to a pressure of about 3 Torr. The spectral profile of the 2^3S_1-2^3P line ($\lambda = 10\,830$ Å) is illustrated in Fig. 6 together with the lamp dimensions. The slight enlargement of diameter at each end of the tube was found to enhance the operation of the discharge. Lamp life and efficiency were highly dependent on careful preparation and use. Prior to filling, the tubes were pumped down to 10^{-6} Torr and baked at 300 °C for 12 h, and a final clean up was effected by 10 min of rf discharge in about 5 Torr of helium. The tube was pumped out again before the final fill of helium was admitted.

The lamp was placed inside a tank circuit coupled to the feed line from a 40-W 100-MHz oscillator. The assembly, together with an Ektron detector for monitoring the lamp intensity, was placed in a box which was open to the atmosphere and projected into the vacuum system from below, so that the lamp itself was only about an inch from the beam. The light was admitted by a Pyrex window and thence passed through a series of slots in the bottom of the microwave cavity. The lamp assembly was cooled by a jet of compressed air.

D. Microwave System

A block diagram of the system is given in Fig. 11. The primary frequency source was a Hewlett-Packard 50-MHz frequency synthesizer which had an inherent stability of 3 in 10^9/day, and was calibrated to an accuracy better than 1 in 10^7. An X-band (8-12 GHz) reflex klystron was phase locked to a harmonic of the synthesizer by means of a Dymec oscillator synchronizer. The latter required a reference frequency in the region of 200 MHz, and this was obtained by means of a step-recovery diode from the fifth harmonic of 40 MHz from the synthesizer. The synthesizer also supplied the 30-MHz i.f. required by the synchronizer.

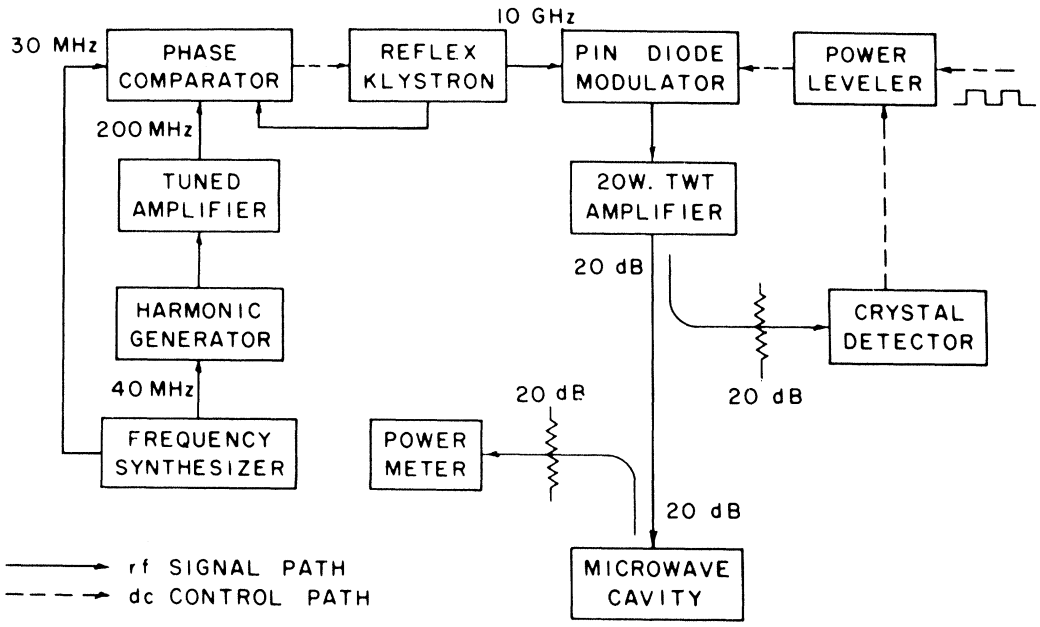

FIG. 11. Block diagram of the microwave system. Solid lines between blocks represent microwave paths, and the broken lines are dc paths for modulation, power leveling, and frequency control.

The output of the phase-locked klystron was fed, after modulation, to a 20-W Varian TWT amplifier which supplied the cavity wherein the 2^3P magnetic resonances were induced. The PIN diode modulator fulfilled two functions: It provided the square-wave modulation required for the two-channel detection system (see I), and also it controlled the average level of power supplied to the cavity. A feedback system was employed to maintain a constant power input to the cavity. The forward power was sampled by a crystal detector whose output went to a leveler amplifier controlling the modulator bias. When the cavity was tuned it was necessary to measure the reverse power, and this was accomplished by a directional coupler and a thermistor power meter.

The microwave cavity is shown in Fig. 10. It was a piece of X-band wave guide, bent into a U with the larger lateral dimension parallel to the plane of the diagram. This configuration provided an oscillatory magnetic field H_1 perpendicular to the z direction when the cavity resonated in the TE_{10n} mode. The apertures were cut as a series of holes, shown in detail at the bottom of the diagram. Unbroken slits would have caused too severe a disruption of the microwave currents. The cavity had an unloaded Q of about 1500.

Two electrical lengths were selectable by inverting the short/spacer and iris/spacer assemblies. A different iris diameter was necessary at each frequency to achieve good coupling (meaning return loss < 20 dB). At the shorter length, modes $n=6$ and 8 resonated at 9.8 and 11.7 GHz, respectively, while at the longer length, modes $n=4, 6$ resonated at 8.8 and 10.9 GHz, respectively.

IV. EXPERIMENTAL PROCEDURE

The 2^3P transition signals were observable as a change in the number of 2^3S_1 ($m_S = 0 \rightarrow \pm 1$) transitions due to application of the resonant microwave field as described in I. These signals could be measured with integrating times of several minutes by means of a two-channel counting system synchronized with square-wave modulation of the microwaves. The self-normalizing feature of this detection scheme meant that the observed signal, to first order, was independent of beam intensity. In the "microwaves-off" channel there was a considerable background from 2^3S_1 atoms which had not undergone optical transitions. This was because of imperfect selection of the $2^3S_1(m_S = 0 \rightarrow \pm 1)$ trajectories, and the percentage signals therefore were somewhat less than calculated. In addition, the presence of the background meant that the observed signal had some direct dependence on the lamp intensity. Also the signal had a direct dependence on the intensity of the microwave field, and it was important for these two parameters to be stable throughout an experimental run.

The resonances were plotted point by point, varying the magnetic field at a fixed microwave frequency, i.e., in Eq. (9) $\omega_{\alpha\beta}$ was varied with ω constant. For each point the "microwaves-off" channel was allowed to run to 10^5 counts, and this took about 10 min. The points were ordered in time as pairs symmetric about the line-shape center, and to first order this canceled the effects of slow drifts in lamp and microwave field intensities.

The proton g factor (in terms of the Bohr magneton) used in converting the NMR field measurements, was taken to be

$$g_p = 3.041\,974\,9 \times 10^{-3} \quad (\pm 0.1\,\text{ppm}), \tag{12}$$

for our sample of mineral oil. This number was obtained by a comparison with a spherical water sample in a high-resolution NMR spectrometer. The value of the g factor in the water sample was assumed to be known accurately,[17] and our results for mineral oil agreed well with published values.[18] A correction of 3 ± 1 ppm was required to allow for the fact that the field was not measured at the exact location of the atomic beam. The quantity $\mu_0 H$ [Eq. (2)], which was used in reducing the data, was expressed directly in terms of the product of the g factor in Eq. (12) and the measured NMR frequency at each field point.

A total of 113 resonance curves were plotted, consisting of transitions 2, 3, 9, 10, and 12 (Fig. 4) at microwave frequencies of 8.8, 10.9, and 11.7 GHz (Fig. 5). Two experimental plots are illustrated in Figs. 12(a) and 12(b) representing, respectively, the smallest and largest signals obtained. The error bars are based solely on counting statistics. The applied microwave frequency was $\nu_{K'}$ and the solid curve is a fitted Lorentzian line shape. The fitting procedure is described in Sec. V.

V. DATA REDUCTION

The quantity $\mu_B H$ was evaluated from the NMR frequency for each experimental data point. This was used to calculate the matrix elements of $\mathcal{H}_Z$ from Table I, and the energy eigenvalue was determined for each of the two sublevels relevant to the transition. The difference between the two eigenvalues gave the 2^3P transition frequency $\nu(^3P, \mu_B H)$ resonant at this value of $\mu_B H$. The $\nu(^3P, \mu_B H)$ were evaluated as pure numbers, with the parameters g_S', g_L', and g_x initially taken to be the known constants g_S, g_L, and 0, respectively; i.e., for the purpose of obtaining a fit to the line shape the contributions of the third term on the right-hand side of Eq. (2) were ignored. We shall refer to these contributions as the "residuals"; and it was from

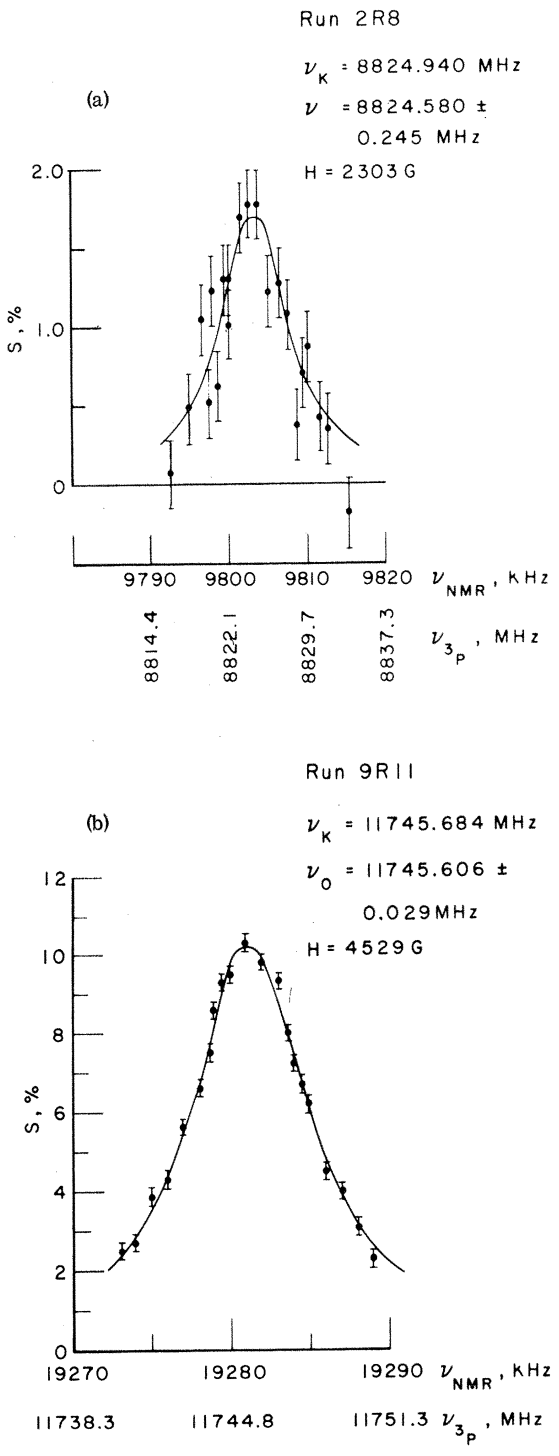

FIG. 12. Typical experimental plots of signal versus magnetic field for (a) transitions 2 and (b) transitions 9. ν_K is the applied microwave frequency; ν_{3_P} is the computed ^3P transition frequency for a value of field given by the NMR frequency. ν_0 is the value of ν_{3_P} at the center of the fitted line shape.

the measured residuals for the various 2^3P transitions that we obtained experimental values for g_s', g_L', and g_x.

The set of points signal S versus $\nu(^3P, \mu_B H)$ were then fitted to the Lorentzian line shape

$$S = A/\{[\nu_0 - \nu(^3P, \mu_B H)]^2 + B\} \tag{13}$$

using the least-squares program described in I. This line shape contained three unknown parameters to be determined from the fit: the height factor A, the width factor B, and the line center ν_0. After ν_0 had been determined, it was compared with the microwave frequency ν_K and the difference $\Delta\nu = (\nu_K - \nu_0)$ presumably represented the experimental value of the residuals for this particular 2^3P transition and frequency. This procedure assumed that the residual part of $\nu(^3P, \mu_B H)$ was the same in all regions of the line shape. It was valid because the residuals comprised less than 1 part in 10^4 of $\nu(^3P, \mu_B H)$. The resonance linewidths, ranging between 5 and 10 MHz, were less than 1 in 10^3 of $\nu(^3P, \mu_B H)$, and hence the change in residuals over an experimental line shape was less than 1 ppm of $\nu(^3P, \mu_B H)$.

Each set of resonances, with a given transition at a particular microwave frequency, constituted a separate measurement of the residuals. The theoretical residuals could be expressed in terms of $(g_S' - g_S)$, $(g_L' - g_L)$, and g_x using the Hamiltonian matrix of Table I. Experimental values of these parameters were obtained by a least-squares fit to the measured residuals from all transitions and frequencies.

The quadratic term $\vec{\mathcal{H}}_Q$ in the Hamiltonian contributed appreciably only to transition 12 (about 2 ppm), based on reasonable estimates of the integrals R_{14} and R_{15} (Appendix B). Our experiment therefore was virtually insensitive to this contribution, and no attempt was made to estimate R_{14} and R_{15} from the experimental data.

VI. RESULTS AND DISCUSSION

In Table II, we summarize the measured residuals $\Delta\nu_i$ for the five transitions at three different microwave frequences. The subscript i refers to a particular field and frequency. Measurements were not made on transitions 2 and 10 at 11.7 GHz. Two sets of experimental uncertainties are included. The number after a ± sign $\bar{\sigma}$ is the combination of statistical (counting) errors from the individual runs. The number in brackets σ^* is the standard deviation of the mean for this set of runs. The fact that the $\bar{\sigma}$, σ^* were comparable in magnitude indicates that random errors arose primarily from counting statistics, and it is therefore doubtful that serious inaccuracies arose from instabilities in lamp and microwave-field intensities.

TABLE II. Measured residuals compared with theory.

	$\Delta\nu_i$ in kHz at a given microwave frequency			Average	Hydrogenic theory
Trans. No.	8.8 GHz	10.9 GHz	11.7 GHz	$(\Delta\nu/\nu)$ ppm	$(\Delta\nu/\nu)$ ppm
9	286±32(27)	391±19(13)	453±15(13)	36.6±1.7	41.8
3	246±30(31)	399±15(14)	398±23(9)	34.1±1.7	33.1
12	452±93(121)	372±34(51)	418±42(18)	35.6±2.7	33.3
10	222±92(88)	272±28(34)		24.1±3.2	31.9
2	132±85(136)	472±25(46)		40.8±3.0	39.4

The over-all accuracy was limited to between 1 and 2 ppm of $\nu(^3P)$ because of a systematic uncertainty in our knowledge of the average value of the magnetic field at the location of the atomic beam. Other possible systematic errors are discussed in Appendix C.

The penultimate column presents the results as an average of $(\Delta\nu/\nu)$, since this parameter should be constant for each transition. The quoted uncertainties are the *combined* statistical and systematic field errors, and are intended to represent one standard deviation. The final column is the theoretical residuals computed using a hydrogenic approximation for the radial wave functions (Appendix B). The accuracy of these hydrogenic values is discussed below.

Our data were fitted to theory independent of any assumptions about radial wave functions (other than the small allowance made for the contribution of $\vec{\mathcal{H}}_Q$). Values for the residuals $\Delta\nu_i^T$ were computed using the Hamiltonian matrix Table I, in terms of the three unknown quantities $(g_S' - g_S)$, $(g_L' - g_L)$, and g_x. The "measured" values of these parameters were determined by minimizing the least-squares sum

$$\sum_i (\Delta\nu_i - \Delta\nu_i^T)^2,$$

where the summation is over the thirteen separate results listed in Table II. The results, compared with the predictions using hydrogenic wave functions, are given in Table III. We note that the most accurate result is for $(g_S' - g_S)$. This is because the frequencies of the transitions with the strongest signals were most sensitive to g_S' for the reasons discussed in Sec. II. The bases for the theoretical limits of error are discussed in Appendix B. It should be noted that the theoretical value of g_x is accidentally small since it arises largely from the subtraction of two nearly equal quantities some five times larger (see Appendix B).

TABLE III. Comparison of experimental and theoretical g factors.

	Experiment (ppm)	Hydrogenic theory (ppm)
$g_S' - g_S$	−76.0±2.4	−79.9±3.5
$g_L' - g_L$	+3.8±9.0	+1.1±1.5
g_x	4.0±25.0	−3.2±4.4

Although there is good agreement between the measured and calculated g factors, the accuracy of the hydrogenic theory is questionable (Appendix B) and an independent assessment of our results should be made. An important consideration is the goodness of fit to the sets of experimental data (Table II.) The χ^2 was 26 for 10 deg of freedom, an unsatisfactory result since this indicates a probability of less than 1%. One might add, however, that 10 deg of freedom represents a small statistical sample, and that enlargement of the experimental error bars by a factor of 1.7 would have given a χ^2 probability of 50%. The poor fit, which is reflected in the experimental uncertainties of Table III, is illustrated also in Fig. 13 where we have compared the fitted fractional residuals with the measurements (Table II) averaged over each transition. The scatter is clearly outside the ex-

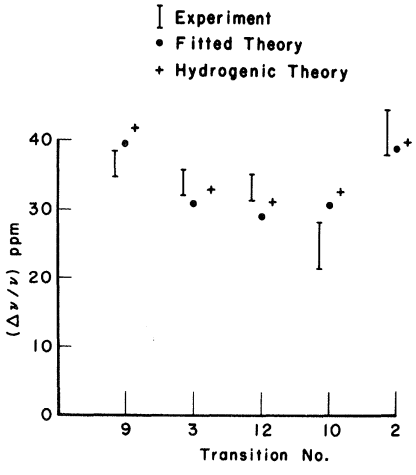

FIG. 13. Experimental fractional residuals for five 2^3P transitions, compared with predictions using fitted g factors, and with g factors calculated from quasihydrogenic radial wave functions.

perimental uncertainties, and if this arose from larger-than-statistical scatter in the individual measurements it would have resulted in wide differences between the $\bar{\sigma}$ and σ^*. Such was not the case. In addition, we emphasize that the scatter is independent of any assumption concerning the radial integrals since these were all included as unknowns in the fitting parameters. A systematic error in field measurement would not have affected the fit, but merely would have moved the whole pattern of Fig. 13 up or down.

The validity of the fitting parameters does depend on the assumption of a pure (sp) configuration used in evaluating the matrix of Table I. The (sp) assumption should be rigorously true unless one considers admixtures of doubly excited configurations. Breakdown of LS coupling is discussed in Appendix C. The contribution of the 2^1P state is very small, but the sum of effects of all other states could be appreciable. Further theoretical work is required.

In any case, to within the limits of experimental errors and the uncertainties indicated by the quality of the fit to all the data, we can conclude the following:

$$g_S = 2.002\,243\,2 \pm 0.000\,002\,4,$$

$$g_L = 0.999\,867 \pm 0.000\,009,$$

$$g_x = -(4.0 \pm 25.0) \times 10^{-6}\ .$$

VII. 2^3P_1–2^3P_2 FINE STRUCTURE

In I, our result for the 2^3P_1-2^3P_2 fine structure separation was quoted with a standard deviation of 0.008 MHz for the "high"-field measurement. This included an uncertainty of 0.007 MHz arising from our estimates of the relativistic and motional corrections to the Zeeman effect. The present work has provided an accurate verification of these corrections, reducing the relevant uncertainty to 0.0025 MHz. Our over-all result for this fine structure may be quoted now as

$$E(2^3P_1 - 2^3P_2) = 2291.196 \pm 0.005\ \text{MHz}. \tag{14}$$

ACKNOWLEDGMENTS

The authors are grateful to Dr. C. E. Johnson for participating in some phases of the design of the apparatus, to Dom Constantino for valiant assistance in the construction, and to Ahovi Kponou for assistance in taking data. One of us (SAL) acknowledges fellowship support by the National Science Foundation.

APPENDIX A: MATRIX ELEMENTS OF THE ZEEMAN HAMILTONIAN

Equations (4) and (5) need to be expressed in a form suitable for determining the matrix elements in an $|LSJm_J\rangle$ representation. Equation (4a) is reduced, following Innes and Ufford,[8] using spherical tensor notation. The results are

$$\vec{\delta}\vec{\mu}_1 = -\alpha^2\mu_B \sum_i (\vec{l}_i + 2\vec{s}_i)\, T_i, \tag{A1}$$

$$\vec{\delta}\vec{\mu}_2 = \tfrac{2}{3}\alpha^2\mu_B \sum_i \frac{1}{r_i}\,(\vec{s}_i + [\tfrac{5}{2}]^{1/2}\{\vec{S}_i\,\vec{C}_i^{(2)}\}^{(1)})\ , \tag{A2}$$

$$\vec{\delta}\vec{\mu}_{3,4} = 2\alpha^2\mu_B \sum_{i<j} \Bigg((\vec{s}_i + 2\vec{s}_j) \sum_k (-)^k (2k+1)^{1/2} \Bigg\{ \frac{1}{3}\left[k\,\frac{r_i^k}{r_j^{k+1}} - (k+1)\right]\frac{r_j^k}{r_i^{k+1}}\ \{\vec{C}_i^{(k)}\,\vec{C}_j^{(k)}\}^{(0)}$$

$$- \frac{[k(k+1)]^{1/2}}{2\sqrt{6}}\left[\frac{r_i^k}{r_j^{k+1}} + \frac{r_j^k}{r_i^{k+1}}\right]\{\vec{C}_i^{(k)}\,\vec{C}_j^{(k)}\}^{(1)} - \frac{[k(k+1)]^{1/2}}{6\sqrt{2}}\left[\left(\frac{2k+3}{2k-1}\right)^{1/2}\frac{r_i^k}{r_i^{k+1}} - \left(\frac{2k-1}{2k+3}\right)^{1/2}\frac{r_j^k}{r_i^{k+1}}\right]\{\vec{C}_i^{(k)}\,\vec{C}_j^{(k)}\}^{(2)}$$

$$+ \frac{1}{2\sqrt{3}}\left(\frac{k(k-1)(2k-3)}{2k-1}\right)^{1/2}\frac{r_i^k}{r_j^{k+1}}\{\vec{C}_i^{(k-2)}\,\vec{C}_j^{(k)}\}^{(2)} - \frac{1}{2\sqrt{3}}\left(\frac{(k+1)(k+2)(2k+5)}{2k+3}\right)^{1/2}\frac{r_j^k}{r_i^{k+1}}\{\vec{C}_i^{(k+2)}\,\vec{C}_j^{(k)}\}^{(2)}\Bigg\}\Bigg)^{(1)}, \tag{A3}$$

$$\vec{\delta}\vec{\mu}_5 = (3)^{-1/2}\alpha^2\mu_B \sum_{i<j}\sum_k (-)^k \Bigg(\left(\frac{r_i^k}{r_j^{k+1}} + \frac{r_i^{k+2}}{r_j^{k+3}}\right)\Bigg\{ \frac{k(k+3)}{2k+3}\,[(2k+1)^{1/2}\{\vec{C}_i^{(k)}\{C_j^{(k)}\vec{l}_j\}^{(k)}\}^{(1)}$$

$$+ (2k+5)^{1/2}\{\vec{C}_i^{(k+2)}\{\vec{C}_j^{(k+2)}\vec{l}_j\}^{(k+2)}\}^{(1)}] - 2\left(\frac{2k+1}{2k+3}\right)^{1/2}\Bigg[(2k+1)^{1/2}\{C_i^{(k)}\{C_j^{(k)}l_j\}^{(k+1)}\}^{(1)}$$

$$+ \left(\frac{(k+1)\ (2k+5)}{k+2}\right)^{1/2}\{\vec{C}_i^{(k+2)}\{\vec{C}_j^{(k)}\vec{l}_j\}^{(k+1)}\}^{(1)}\Bigg]\Bigg\} + \left((k+3)\,\frac{r_i^{k+2}\,r_j}{r_j^{k+2}} - k\,\frac{r_j^{k+1}\,\partial r_j}{r_i^{k+1}}\right)\frac{1}{2k+3}$$

$$\times\{[k(k+1)\ (2k+1)]^{1/2}\{C_i^{(k)}C_j^{(k)}\}^{(1)} - [(k+2)\ (k+3)\ (2k+5)]^{1/2}\{C_i^{(k+2)}C_j^{(k+2)}\}^{(1)}\}\Bigg). \tag{A4}$$

$\vec{C}_i^{(k)}$ is the spherical tensor[19] of rank k for the ith electron. The $\vec{s}_i$, $\vec{l}_i$ represent, respectively, spin and

orbital angular momentum operators (rank 1) for the ith electron. A term such as $\{\vec{C}_i^{(k)}, \vec{C}_i^{(k')}\}^{(K)}$ represents the coupling[19] of the tensors $\vec{C}_i^{(k)}$, $\vec{C}_j^{(k')}$ to form a tensor of rank K. r_i is the radial coordinate of the ith electron, and ∂r_i is an abbreviation for $\partial/\partial r_i$. $\alpha\,(=e^2/\hbar c)$ is the fine structure constant. Factors such as $r_i^k/r_j^{k'}$ imply that $r_i \leq r_j$. The radial operators are expressed in atomic units.

In a similar way, we have recoupled Eq. (4b) in the form

$$\delta\mu_6 = -2\frac{m}{M}\,\mu_B \sum_{i<j}\left(2\frac{r_i}{r_j}\{\vec{C}_i^{(1)}\{\vec{C}_j^{(1)}\vec{1}_j\}^{(1)}\} - \sqrt{2}\, r_i \partial r_j \{C_i^{(1)} C_j^{(1)}\}^{(1)}\right), \tag{A5}$$

where m, M, are, respectively, the electronic and nuclear masses. Finally, the recoupled version of $\vec{\mathcal{H}}_Q$, Eq. (5) can be expressed as

$$\vec{\mathcal{H}}_Q = \frac{1}{6}\frac{(\mu_B H)^2}{R_\infty}\sum_i (1 - C_{i_0}^{(2)})\, r_i^2, \tag{A6}$$

where R_∞ is the Rydberg constant.

The matrix elements of $(\delta\mu_r)_z$ are required in the scheme $|LSJm_J\rangle$. We now specialize to the case of a ^3P state of the two-electron atom, where the total wave function, with respect to interchange of the two electrons, is antisymmetric in spatial coordinates and symmetric in spin coordinates. Further, we assume that each radial component of the antisymmetrized spatial part of the wave function can be written as a product of components for each electron $R_{1s}(r_i)$ and $R_{2p}(r_j)$. The matrix elements are given below where we have included, for comparison, the elements of the first two terms of Eq. (2). The vector-coupling coefficients are given in the standard n-J symbol notation[19]:

$$\langle {}^3P_J m_J | g_L \mu_B \vec{L}\cdot\vec{H} + g_S \mu_B \vec{S}\cdot\vec{H} | {}^3P_{J'} m_{J'}\rangle = \sqrt{6}\,\mu_B H \times (-)^{1-m_J}[(2J+1)(2J'+1)]^{1/2}$$
$$\times \begin{pmatrix} J & 1 & J' \\ -m_J & 0 & m_J \end{pmatrix} \begin{Bmatrix} J & 1 & J' \\ 1 & 1 & 1 \end{Bmatrix} [(-)^{J+J'} g_L + g_S], \tag{A7}$$

$$\langle {}^3P_J m_J | \vec{\delta}\vec{\mu}_1 \cdot \vec{H} | {}^3P_{J'} m_{J'}\rangle = -\sqrt{6}\,\alpha^2 \mu_B H \times (-)^{1-m_J}[(2J+1)(2J'+1)]^{1/2}$$
$$\times \begin{pmatrix} J & 1 & J' \\ -m_J & 0 & m_J \end{pmatrix} \begin{Bmatrix} J & 1 & J' \\ 1 & 1 & 1 \end{Bmatrix} [R_1 + [1 + (-1)^{J+J'}] R_2], \tag{A8}$$

$$\langle {}^3P_J m_J | \vec{\delta}\vec{\mu}_2 \cdot \vec{H} | {}^3P_{J'} m_{J'}\rangle = \sqrt{6}\,\alpha^2 \mu_B H \times (-)^{1-m_J}[(2J+1)(2J'+1)]^{1/2}$$
$$\times \begin{pmatrix} J & 1 & J' \\ -m_J & 0 & m_J \end{pmatrix} \left(\frac{1}{3}\begin{Bmatrix} J & 1 & J' \\ 1 & 1 & 1 \end{Bmatrix}(R_3 + R_4) + (-)^J \begin{Bmatrix} 1 & 1 & 2 \\ 1 & 1 & 1 \\ J & J' & 1 \end{Bmatrix} R_4\right), \tag{A9}$$

$$\langle {}^3P_J m_J | (\vec{\delta}\vec{\mu}_3 + \vec{\delta}\vec{\mu}_4)\cdot\vec{H} | {}^3P_{J'} m_{J'}\rangle = \sqrt{6}\,\alpha^2 \mu_B H \times (-)^{J-m_J}[(2J+1)(2J'+1)]^{1/2}$$
$$\times \begin{pmatrix} J & 1 & J' \\ -m_J & 0 & m_J \end{pmatrix}\left[\begin{Bmatrix} 1 & 1 & 2 \\ 1 & 1 & 1 \\ J & J' & 1 \end{Bmatrix}\left(\tfrac{3}{2}R_6 + 2R_7 - \tfrac{3}{2}R_8\right) + \begin{Bmatrix} 1 & 1 & 0 \\ 1 & 1 & 1 \\ J & J' & 1 \end{Bmatrix}\left(R_7 - \tfrac{3}{2}R_6 - \tfrac{3}{2}R_5\right)\right], \tag{A10}$$

$$\langle {}^3P_J m_J | \vec{\delta}\vec{\mu}_5 \cdot H | {}^3P_{J'} m_{J'}\rangle = \sqrt{6}\,\alpha^2 \mu_B H \times (-)^{J+J'+1-m_J}[(2J+1)(2J'+1)]^{1/2}$$
$$\times \begin{pmatrix} J & 1 & J' \\ -m_J & 0 & m_J \end{pmatrix} \begin{Bmatrix} J & 1 & J' \\ 1 & 1 & 1 \end{Bmatrix} (-\tfrac{1}{3}R_5 + \tfrac{2}{15}R_7 - \tfrac{1}{3}R_8 + \tfrac{2}{15}R_9 + \tfrac{1}{30}R_{10} - \tfrac{1}{30}R_{11} - \tfrac{2}{15}R_{12} + \tfrac{2}{15}R_{13}),$$

$$\langle {}^3P_J m_J | \vec{\delta}\vec{\mu}_6 \cdot \vec{H} | {}^3P_{J'} m_{J'}\rangle = \sqrt{6}\,\mu_B H \frac{m}{M} \times (-)^{1-m_J+J+J'}[(2J+1)(2J'+1)]^{1/2}$$
$$\times \begin{pmatrix} J & 1 & J' \\ -m_J & 0 & m_J \end{pmatrix} \begin{Bmatrix} J & 1 & J' \\ 1 & 1 & 1 \end{Bmatrix} (\tfrac{1}{3}R_{16} - \tfrac{1}{3}R_{17} + \tfrac{2}{3}R_{18}), \tag{A12}$$

$$\langle {}^3P_J m_J | \vec{\mathcal{H}}_Q | {}^3P_{J'} m_{J'}\rangle = (-)^{J+J'-m_J}\frac{(\mu_B H)^2}{2\sqrt{3}\,R_\infty}[(2J+1)(2J'+1)]^{1/2}$$
$$\times \left[\begin{pmatrix} J & 0 & J' \\ -m_J & 0 & m_J \end{pmatrix}\begin{Bmatrix} J & 0 & J' \\ 1 & 1 & 1 \end{Bmatrix}(R_{14} + R_{15}) + (\tfrac{2}{5})^{1/2}\begin{pmatrix} J & 2 & J' \\ -m_J & 0 & m_J \end{pmatrix}\begin{Bmatrix} J & 2 & J' \\ 1 & 1 & 1 \end{Bmatrix} R_{15}\right], \tag{A13}$$

where the radial integrals R_1–R_{18} are discussed in Appendix B. We make the following groupings:

$$g'_L = g_L + \alpha^2\left(-R_2 - \tfrac{1}{3}R_5 + \tfrac{2}{15}R_7 - \tfrac{1}{3}R_8 + \tfrac{2}{15}R_9 + \tfrac{1}{30}R_{10} - \tfrac{1}{30}R_{11} - \tfrac{2}{15}R_{12} + \tfrac{2}{15}R_{13}\right) + \frac{m}{M}\left(\tfrac{1}{3}R_{16} - \tfrac{1}{3}R_{17} + \tfrac{2}{3}R_{18}\right), \tag{A14}$$

$$g'_S = g_S + \alpha^2\left(-R_1 - R_2 + \tfrac{1}{3}R_3 + \tfrac{1}{3}R_4 - \tfrac{1}{2}R_5 - \tfrac{1}{2}R_6 + \tfrac{1}{3}R_7\right), \quad g_x = \alpha^2\left(R_4 - \tfrac{3}{2}R_6 - 2R_7 + \tfrac{3}{2}R_8\right)$$

When we have matrix elements of $\vec{\mathcal{H}}_Z$, Eq. (2) becomes

$$\langle {}^3P_J m_J | \vec{\mathcal{H}}_Z | {}^3P_{J'} m_J \rangle = (-)^{1-m_J}\left[(2J+1)(2J'+1)\right]^{1/2}\begin{pmatrix} J & 1 & J' \\ -m_J & 0 & m_J \end{pmatrix} \times\sqrt{6}\left[\begin{Bmatrix} J & 1 & J' \\ 1 & 1 & 1 \end{Bmatrix}\left[g'_S + (-)^{J+J'} g'_L\right](-)^J g_x \begin{Bmatrix} 1 & 1 & 2 \\ 1 & 1 & 1 \\ J & J' & 1 \end{Bmatrix}\right]\mu_B H. \tag{A15}$$

Finally, we have for the matrix elements of $\vec{\mathcal{H}}_Q$

$$\langle {}^3P_J m_J | \vec{\mathcal{H}}_Q | {}^3P_{J'} m_J \rangle = (-)^{J+J'-m_J}\left[(2J+1)(2J'+1)\right]^{1/2}\left[\begin{pmatrix} J & 0 & J' \\ -m_J & 0 & m_J \end{pmatrix}\begin{Bmatrix} J & 0 & J' \\ 1 & 1 & 1 \end{Bmatrix} \times\left(R_{14} + R_{15}\right) + \left(\tfrac{2}{5}\right)^{1/2}\begin{pmatrix} J & 2 & J' \\ -m_J & 0 & m_J \end{pmatrix}\begin{Bmatrix} J & 2 & J' \\ 1 & 1 & 1 \end{Bmatrix} R_{15}\right]\frac{1}{2\sqrt{3}}\frac{(\mu_B H)^2}{R_\infty}. \tag{A16}$$

These matrix elements have been evaluated for the relevant J, J', m_J, and are listed in Table I.

APPENDIX B: RADIAL INTEGRALS

The radial part of the antisymmetrized 2^3P wave function is written

$$R(r_1, r_2) = 2^{-1/2}\{R_s(r_1)R_p(r_2) - R_p(r_1)R_s(r_2)\}, \tag{B1}$$

where $R_s(r)$, $R_p(r)$, respectively, refer to the components due to the s and p electrons. It is necessary to write $R(r_1, r_2)$ in a product form, since the angular matrix elements evaluated in the preceding Appendix A involved single-electron operators. We believe that Eq. (B1) is sufficiently generalized, since configuration mixing cannot change the sp character of the ^3P state in helium, and any other admixtures would be entirely negligible for our purpose.

A typical radial integral appearing in the matrix elements of Appendix A is of the form

$$R_a = \tfrac{1}{2}\int_0^\infty \int_0^{r_2} R^*(r_1, r_2)\vec{f}_a \times R(r_1, r_2) r_1^2 r_2^2 dr_1 dr_2. \tag{B2}$$

The $\vec{f}_a(r_1, r_2)$ may contain differential operators and may have the stipulation $r_1 \leq r_2$. Substituting Eq. (B1) into (B2), and making self-explanatory abbreviations, we have

$$R_a = \tfrac{1}{2}\{\langle sp|f_a|sp\rangle + \langle ps|f_a|ps\rangle - \langle sp|f_a|ps\rangle - \langle ps|f_a|sp\rangle\}. \tag{B3}$$

The integrals involved in the matrix elements of Appendix A are listed in Table IV.

We have made numerical estimates of the integrals R_1, R_2, R_3, and R_4 using the modified hydrogenic wave functions

$$R_s = 2Z_1^{3/2} e^{-Z_1 r}, \qquad Z_1 = 1.99,$$
$$R_p = (24)^{-1/2} Z_2^{5/2} r e^{-Z_2 r/2}, \quad Z_2 = 1.09. \tag{B4}$$

The values of the "effective" atomic numbers Z_1 and Z_2 are chosen on the basis of a variational calculation of the 2^3P energy.[20] The units of r are the

TABLE IV. Integrals involved in the matrix elements of Appendix A.

$R_1 = \langle sp \mid T_1 \mid sp\rangle$	~ 1.98
$R_2 = \langle ps \mid T_1 \mid ps\rangle$	~ 0.149
$R_3 = \langle sp \mid 1/r_1 \mid sp\rangle$	~ 1.99
$R_4 = \langle ps \mid 1/r_1 \mid ps\rangle$	~ 0.272
$R_5 = \langle sp \mid 1/r_1 \mid sp\rangle (r_2 \leq r_1)$	$\sim 3.3\times10^{-3}$
$R_6 = \langle ps \mid 1/r_1 \mid ps\rangle (r_2 \leq r_1)$	~ 0.246
$R_7 = \langle ps \mid r_1/r_2^2 \mid sp\rangle$ $= \langle sp \mid r_1/r_2^2 \mid ps\rangle (r_1 \leq r_2)$	$\sim 5.7\times10^{-3}$
$R_8 = \langle sp \mid r_1^2/r_2^3 \mid sp\rangle (r_1 \leq r_2)$	~ 0.020
$R_9 = \langle ps \mid r_1^3/r_2^4 \mid sp\rangle$ $= \langle sp \mid r_1^3/r_2^4 \mid ps\rangle (r_1 \leq r_2)$	$\sim 2.0\times10^{-3}$
$R_{10} = \langle ps \mid r_2^2 \partial r_2/r_1^2 \mid sp\rangle (r_2 \leq r_1)$	$\sim 1.2\times10^{-3}$
$R_{11} = \langle sp \mid r_2^2 \partial r_2/r_1^2 \mid ps\rangle (r_1 \geq r_2)$	$\sim -1.6\times10^{-3}$
$R_{12} = \langle sp \mid r_1^3 \partial r_2/r_2^3 \mid sp\rangle (r_2 \geq r_1)$	$\sim 0.5\times10^{-3}$
$R_{13} = \langle sp \mid r_1^3 \partial r_2/r_2^3 \mid ps\rangle (r_1 \leq r_2)$	$\sim 4.9\times10^{-3}$
$R_{14} = \langle sp \mid r_1^2 \mid sp\rangle$	~ 0.76
$R_{15} = \langle ps \mid r_1^2 \mid ps\rangle$	~ 25.2
$R_{16} = \langle ps \mid r_1 \partial r_2 \mid sp\rangle$	~ 0.0174
$R_{17} = \langle sp \mid r_1 \partial r_2 \mid ps\rangle$	~ -0.102
$R_{18} = \langle ps \mid r_1/r_2 \mid sp\rangle$ $= \langle sp \mid r_1/r_2 \mid ps\rangle$	~ 0.0423

∂r_2 means $\partial/\partial r_2$

Bohr radius $a_0=\hbar^2/me^2$. Estimates of the radial integrals using Eq. (B4) are also listed in Table IV. The wave functions Eq. (B4) give a value for the energy of the 2^3P state to within 2%,[20] and hence we expect this extent of accuracy for R_1, R_2, R_3, and R_4, which are essentially energy integrals. The remaining integrals would be much less accurate. As an example, we have compared the p-electron integral of r^{-3} with the results of a very accurate variational calculation,[21] and find that the use of Eq. (B4) is apparently in error by about 50%.

We have nevertheless calculated the remaining integrals using Eq. (B4) with $Z_1=2$ and $Z_2=1$. R_5 and R_6 are similar to the energy integrals R_1–R_4, although the contribution of electron correlation would differ to some extent owing to the restrictions on r_1, r_2. The integral R_9 would diverge using Eq. (B4) because of the absence of electron correlation, and the value assigned in Table IV is an extrapolation from similar integrals. If one assumes that these estimates give some idea of orders of magnitude for R_7–R_{18}, it is reasonable to conclude that about 90% of the corrections to the Zeeman effect arise from the more accurate R_1–R_6.

In Table V, we summarize the contributions of the various radial integrals to the factors $(g_S'-g_S)$, $(g_L'-g_L)$, and g_X. The uncertainties quoted for the theoretical values of these numbers and those in Table III are based on the assumption of 3% errors in R_1–R_4, 20% in R_5, R_6, and 100% for the remaining integrals.

APPENDIX C: SYSTEMATIC EXPERIMENTAL EFFECTS

We summarize here an assessment of the systematic quantities which could have affected the accuracy of our experiment.

A. Singlet Admixture

Magnetic interactions, such as spin-orbit coupling between states of the same J, lead to a partial breakdown of the L-S approximation. In the case of 2^3P, the largest contribution arises from 2^1P admixture, leading to a shift of about 5 MHz[22] in the energy of the 2^3P_1 state, which thereby constitutes part of the measured fine structure. The 2^1P lies some 6×10^7 MHz above the 2^3P, and the lowest-order contribution to the Zeeman effect are third-order perturbations of the form

$$\Delta E\ (\text{Zeeman}) \sim \frac{\langle {}^3P_1|\,\text{spin orbit}\,|{}^1P_1\rangle^2\langle {}^1P_1|\,\text{Zeeman}\,|{}^1P_1\rangle}{[E(2^3P)-E(2^1P)]^2}$$

$$\sim 10^{-4}\ \text{MHz}. \qquad \text{(C1)}$$

This was more than an order of magnitude smaller than our experimental uncertainties. Lower-order perturbation terms do not arise, since the Zeeman Hamiltonian is diagonal in L,S. The contributions of terms such as Eq. (C1) are more than an order of magnitude smaller than our other uncertainties.

B. Slope Correction

This is an apparent shift in the center of an experimental line shape arising from asymmetries caused by the variation of the optical excitation and decay probabilities as the field is swept through the resonance. A detailed discussion of the correction has been given in I. At the high magnetic fields used in the present work, the resonances spanned only about 1 in 10^3 of the total field, and the slope

TABLE V. Contributions to theoretical g factors.

Term	Theoretical g_S' source	Value$\times10^6$	Term	Theoretical g_L' source	Value$\times10^6$
$-\alpha^2R_1$	$\delta\mu_1$	−105.5	$-\alpha^2R_2$	$\delta\mu_1$	−7.9
$-\alpha^2R_2$	$\delta\mu_1$	−8.0	$-\alpha^2\frac{1}{3}R_8$	$\delta\mu_5$	−0.4
$\alpha^2\frac{1}{3}R_3$	$\delta\mu_2$	35.4	$\frac{m}{M}\frac{1}{3}R_{16}$	$\delta\mu_6$	0.8
$\alpha^2\frac{1}{3}R_4$	$\delta\mu_2$	4.8	$-\frac{m}{M}\frac{1}{3}R_{17}$	$\delta\mu_6$	4.7
$-\alpha^2\frac{1}{2}R_5$	$\delta\mu_{3,4}$	−0.1	$\frac{m}{M}\frac{2}{3}R_{18}$	$\delta\mu_6$	3.9
$-\alpha^2\frac{1}{2}R_6$	$\delta\mu_{3,4}$	−6.6		Theoretical g_x	
$\alpha^2\frac{1}{3}R_7$	$\delta\mu_{3,4}$	0.1	α^2R_4	$\delta\mu_2$	14.6
			$-\alpha^2\frac{3}{2}R_6$	$\delta\mu_{3,4}$	−19.7
			$-2\alpha^2R_7$	$\delta\mu_{3,4}$	0.3
			$\alpha^2\frac{3}{2}R_8$	$\delta\mu_{3,4}$	1.6

Theoretical $g_S'=g_S-(79.9\times10^{-6})=2.002\,239\,3\ (35)$
$g_L'=g_L+(1.1\times10^{-6})=0.999\,864\,0\ (15)$
$g_x=-0.000\,003\,2\ (44)$

corrections amounted to less than 1 in 10^7.

C. Doppler Shift

The fields in the microwave cavity consisted of two oppositely directed running waves. The atomic beam was moving in the direction of one of these and there were Doppler shifts in frequency of order v/λ_g, where v is the atomic velocity and λ_g is the guide wavelength. The shifts for each wave were equal and opposite. For a given velocity, the contribution to the experimental line shape was therefore two slightly separated Lorentzians of equal height. For atoms with the most probable velocity the separation was about 1% of the experimental linewidth. It can be shown quite easily that the composition of two such Lorentzians results in a Lorentzian whose peak height is the sum of the peaks of the components, and whose center frequency is the mean center of the components. The width is identical to the widths of the components to first order in the fraction (separation/linewidth). This effect made no appreciable contribution to our experimental results.

D. Nearby $^3S_1$ Resonance

The metastable 2^3S_1 Zeeman transition frequency lies closest to that of 2^3P transition 9 (Fig. 1). The tail of this resonance could conceivably cause asymmetries in the 2^3P line shapes. The 2^3S resonance had a power-broadened linewidth of about 5 MHz and an intensity approximately 100 times that of a typical 2^3P resonance. The nearest 2^3P transition was separated by 900 MHz and the 2^3S tail contributed about 0.006 of the 2^3P peak signal. The variation of the 2^3S tail over the 2^3P line shape was less than 1 in 10^4 of the signal, and hence this effect was disregarded.

The reader is referred to I for detailed discussions of light shifts, the Bloch-Siegert effect, and variation of microwave-field intensity over the interaction region. None of these effects had appreciable significance in the present work.

---

*Research supported in part by the U.S. Air Force Office of Scientific Research, under Grant Nos. AFOSR 249-66, 249-67, 249-68, and 249-69.

†Present address: Crocker Nuclear Laboratory, University of California, Davis, Calif. 95616; research submitted in partial fulfillment of the requirements for the Ph.D. degree.

‡Present address: Department of Physics and Astronomy, University of Massachusetts, Amherst, Mass. 01002.

[1]F. M. J. Pichanick, R. D. Swift, C. E. Johnson, and V. W. Hughes, Phys. Rev. 169, 55 (1968).

[2]S. A. Lewis, F. M. J. Pichanick, A. Kponou, and V. W. Hughes, Bull. Am. Phys. Soc. 14, 83 (1969).

[3]W. Perl and V. W. Hughes, Phys. Rev. 91, 842 (1953).

[4]W. Perl, Phys. Rev. 91, 852 (1953); see also V. W. Hughes, in *Recent Research in Molecular Beams*, edited by I. Esterman (Adademic, New York, 1959).

[5]A. Abragam and J. H. van Vleck, Phys. Rev. 92, 1448 (1953).

[6]C. W. Drake, V. W. Hughes, A. Lurio, and J. A. White, Phys. Rev. 112, 1627 (1958).

[7]Experiment, H. E. Radford, V. W. Hughes, and V. Beltrán-López, Phys. Rev. 123, 153 (1961); theory, V. Beltrán-López, E. Ley Koo, N. Segovia, and E. Blaisten, *ibid.* 172, 44 (1968).

[8]Experiment, E. B. Rawson and R. Beringer, Phys. Rev. 88, 677 (1952); H. E. Radford and V. W. Hughes, *ibid.* 114, 1274 (1959); theory, F. R. Innes and C. W. Ufford, *ibid.* 111, 194 (1958).

[9]M. L. Perl, I. I. Rabi, and B. Senitsky, Phys. Rev. 98, 611 (1955).

[10]See, for instance, N. Ramsey, *Molecular Beams* (Oxford U.P., New York, 1956); or P. Kusch and V. W. Hughes, in *Encyclopedia of Physics*, edited by S. Flügge (Springer-Verlag, Berlin, 1959), Vol. 37/1.

[11]H. A. Bethe and E. E. Salpeter, *Quantum Mechanics of One- and Two-Electron Atoms* (Springer-Verlag, Berlin, 1957), Sec. 40.

[12]W. E. Lamb, Jr., Phys. Rev. 105, 559 (1957).

[13]The value of (E_1-E_2) is taken from Pichanick *et al.* Ref. 1, while that of (E_0-E_1) is from a forthcoming paper, A. Kponou, C. E. Johnson, F. M. J. Pichanick, S. A. Lewis, and V. W. Hughes, Phys. Rev. (to be published), referred to as III. See also A. Kponou *et al.*, Bull. Am. Phys. Soc. 15, 488 (1970).

[14]C. M. Sommerfield, Ann. Phys. (N.Y.) 5, 26 (1958).

[15]A. Rich, Phys. Rev. Letters 20, 967 (1968).

[16]M. Phillips, Phys. Rev. 76, 18[illegible]949).

[17]T. Myint, D. Kleppner, N. F. Ramsey, and H. G. Robinson, Phys. Rev. Letters 17, 405 (1966).

[18]H. Gutowsky and R. E. McClure, Phys. Rev. 81, 276 (1951).

[19]See, for instance, B. R. Judd, *Operator Techniques in Atomic Spectroscopy* (McGraw-Hill, New York, 1963).

[20]See, for instance, Ref. 11, p. 158.

[21]C. Schwartz, Phys. Rev. 134, A1181 (1964).

[22]G. Araki, M. Ohta, and K. Mano, Phys. Rev. 116, 651 (1959); B. Schiff, C. L. Pekeris, and H. Lifson, *ibid.* 137, A1672 (1965).